

# Unusual d-electron heavy-fermion behaviour in f-electron ferromagnetic antiperovskite $Gd_3SnC$

**Joonho Bang**

Sungkyunkwan University <https://orcid.org/0000-0002-9455-5378>

**Jongho Park**

Sungkyunkwan University

**Kimoon Lee**

Kunsan National University

**Minsoo Kim**

Center for Correlated Electron Systems, Institute for Basic Science <https://orcid.org/0000-0002-4137-4610>

**Wonshik Kyung**

Seoul National University <https://orcid.org/0000-0001-8750-5471>

**Jonathan Denlinger**

Lawrence Berkeley National Lab <https://orcid.org/0000-0001-7645-1631>

**Yeong Kwan Kim**

Korea Advanced Institute of Science and Technology

**Young Hee Lee**

Institute for Basic Science <https://orcid.org/0000-0001-7403-8157>

**Changyoung Kim**

Seoul National University <https://orcid.org/0000-0003-0555-2341>

**Sung Wng Kim** (✉ [kimsungwng@skku.edu](mailto:kimsungwng@skku.edu))

Sungkyunkwan University <https://orcid.org/0000-0002-4802-5421>

---

## Article

**Keywords:** stable antistructures, heavy-fermion behaviour, ferromagnetic gadolinium lattice,  $Gd_3SnC$  antiperovskite

**Posted Date:** March 25th, 2021

**DOI:** <https://doi.org/10.21203/rs.3.rs-336915/v1>

**License:**   This work is licensed under a Creative Commons Attribution 4.0 International License.

[Read Full License](#)

Loading [MathJax]/jax/output/CommonHTML/fonts/TeX/fontdata.js

# Abstract

Inverted structures of common crystal lattices, referred to as antistructures, are rare in nature due to their thermodynamic constraints imposed by the switched cation and anion positions in reference to the original structure. However, a stable antistructure formed with mixed bonding characters of constituent elements in unusual valence states can provide unexpected material properties. Here, we report a heavy-fermion behaviour of ferromagnetic gadolinium lattice in  $\text{Gd}_3\text{SnC}$  antiperovskite, contradicting the common belief that ferromagnetic gadolinium cannot be a heavy-fermion system. The specific heat shows an unusually large Sommerfeld coefficient of  $\sim 1114 \text{ mJ}\cdot\text{mol}^{-1}\cdot\text{K}^{-2}$  with a logarithmic behaviour of non-Fermi-liquid state. We demonstrate that the heavy-fermion behaviour in the non-Fermi-liquid state appears to arise from the hybridized electronic states of gadolinium 5d-electrons participating in metallic Gd–Gd and covalent Gd–C bonds. These results accentuate unusual chemical bonds in  $\text{CGd}_6$  octahedra with the dual characters of gadolinium 5d-electrons for the emergence of heavy-fermions.

## Introduction

The crystal structure constructed with chemical bonds of constituent elements determines the electronic structure of a material and its properties. In a fixed symmetry, electronically inverted structures with switched crystallographic positions of cations and anions from the original structure often have a reversed compositional ratio, which necessarily forms a different coordinated substructure with additional bonding characters and can lead to an exotic electronic structure. However, in general, such antistructures composed of the same constituent elements in the reversed compositional ratio are thermodynamically unstable. Indeed, due to the thermodynamic constraints, antistructures found in several classes of materials are constructed by subsidiary chemical bonds of different constituent elements from original structures. This appears, for example, in the Cd-deficient  $\text{Cd}_3\text{As}_2$  antiferrofluorite<sup>1</sup>, which has a strong covalent bonding nature in a reversed compositional ratio from the ionic  $\text{CaF}_2$  fluorite. It is noteworthy that the  $\text{Cd}_3\text{As}_2$  antiferrofluorite exhibits exotic properties: a three-dimensional topological Dirac band<sup>1–3</sup> along with negative magnetoresistance<sup>4</sup>, anomalous Hall effect<sup>5</sup>, and pressure-induced superconductivity<sup>6</sup>.

$\text{ABX}_3$  perovskites, as the largest family of crystalline materials, also have their counterpart antistructures,  $\text{A}_3\text{BX}$  antiperovskites<sup>7</sup>. In contrast to the perovskite compounds constructed by the ionic bonds of constituent elements in stable valence states, the antiperovskites have mixed bonding characters with ionic, covalent, and metallic bonds in unusual valence states<sup>8</sup>. However, oxide antiperovskites ( $\text{A}_3\text{BO}$ ), antistructures of common oxide perovskites ( $\text{ABO}_3$ ), are hardly stabilized in ambient conditions as oxygen tends to form ionic bonds with counter-cationic  $A$  and  $B$  elements due to its large ionicity<sup>9</sup>. This constraint may be lifted for s-block and transition metal-based antiperovskites, in which additional covalent and metallic bonds come into play for their crystallographic stability<sup>7,10</sup>. The boundary for such stable antiperovskite compounds can be extended to f-block lanthanides, which form a crystal with

various elemental groups of d-block transition metals and p-block post-transition metals<sup>7</sup>. Those compounds may exhibit diverse electronic properties because of the multiple bonding characters with enhanced covalency and/or metallicity. Furthermore, considering the fact that f-electrons often contribute to strongly correlated electronic properties, a variety of unconventional quantum phenomena may be anticipated in f-block antiperovskites, which can exhibit exotic electronic band structures arising from the mixed chemical bonds. However, thermodynamically stable f-block element-based antiperovskites and their novel properties have been hardly demonstrated up to now<sup>7,11</sup>. Herein, we demonstrate the unprecedented heavy-fermion behaviour of the ferromagnetic (FM) gadolinium lattice in the Gd<sub>3</sub>SnC antiperovskite structure and verify the crucial role of the metallic Gd–Gd and covalent Gd–C bonds of CGd<sub>6</sub> octahedral skeleton on an unusually hybridized Gd 5d-electrons responsible for the emergent heavy-fermions.

## Results

**Synthesis and structural analysis.** Figure 1a shows that the Gd<sub>3</sub>SnC crystallizes in the antiperovskite structure (space group:  $Pm\bar{3}m$ ) with face-centred Gd and body-centred C atoms in a Sn cubic lattice, as confirmed by Rietveld analysis of powder X-ray diffraction (XRD) pattern (Supplementary Table 1). Single-phase bulk Gd<sub>3</sub>SnC was synthesized via the melt-solidification process at one atmosphere. This indicates the thermodynamic stability of Gd<sub>3</sub>SnC antiperovskite, which gets additional support from the calculated phonon dispersions having no imaginary frequency (Supplementary Fig. 1). In contrast to the  $ABX_3$  perovskite, which has cation-centred  $BX_6$  octahedra with ionic bonds, Gd<sub>3</sub>SnC has anion-centred CGd<sub>6</sub> octahedra with strong covalent Gd–C and metallic Gd–Gd bonds. This mixed bonding character of Gd bonds in CGd<sub>6</sub> octahedra results in different Gd orbital levels from those of the Gd element and its ionic compounds. As shown in Fig. 1b, while Gd metal and Gd<sub>2</sub>O<sub>3</sub> have ordinary Gd orbital levels of Gd–Gd metallic and Gd–O ionic bonds, respectively, Gd<sub>3</sub>SnC has unusual energy levels for Gd orbitals due to the coexistence of metallic and covalent bonds. Considering the shorter Gd–Gd bond length (3.48 Å) in CGd<sub>6</sub> octahedra compared to that of Gd metal (~ 3.6 Å), one expects an enhanced metallicity and thus additional Fermi level ( $E_F$ ) crossings for Gd bands in Gd<sub>3</sub>SnC. On the other hand, the electronegativity difference between Gd and C is much smaller than that between Gd and O, resulting in the formation of covalent bonds between Gd and C. The energy difference between bonding and antibonding states of the covalent bonds is expected to be significantly smaller than that of ionic bonds between Gd and O. These mixed bonding characters of Gd valence orbitals in CGd<sub>6</sub> octahedra can lead to a peculiar molecular orbital diagram with both metallic and covalent bonds as shown in Fig. 1b. Such observation indicates that Gd<sub>3</sub>SnC antiperovskite may exhibit unusual physical properties that are hardly found in elemental Gd and conventional Gd-related compounds.

**Tricritical ferromagnetic behaviour.** Figure 2a shows the FM phase transition of Gd<sub>3</sub>SnC with a Curie temperature ( $T_C$ ) of 100 K under a low magnetic field ( $H$ ) of 0.1 kOe. In comparison to the itinerant FM in

Gd metal with a  $T_C$  of 297 K, different aspects of the FM order are observed<sup>12</sup>. A sharp increase in the magnetization ( $M$ ) near the  $T_C$  indicates a first-order transition, which is further evidenced by the hysteresis in the temperature ( $T$ ) dependence of electrical resistivity ( $\rho$ ) (Fig. 2e) and the negative slope in the  $M^2$  dependence of  $H/M$  (Supplementary Fig. 2e). In addition, no structural phase transition is observed around the  $T_C$ , indicating that the FM ordering occurs while preserving the antiperovskite structure (Supplementary Fig. 3). We confirm the saturation magnetic moment of  $\sim 6.8 \mu_B$  per Gd obtained from the  $M-H$  curve (Fig. 2b), indicating this FM state comes mostly from the seven Gd 4f-electrons. A notable aspect of  $M(T)$  is a slight decrease in the ZFC curve below  $\sim 20$  K (inset of Fig. 2a), which suggests a possible formation of singlets such as Kondo singlet<sup>13,14</sup>, as will be discussed in the following sections. This unusual behaviour in  $M$  indicates that the near  $E_F$  states of Gd, which do not have contributions from fully localized f-orbitals, may be different from those of the familiar FM Gd metal and Gd-based compounds<sup>12,15</sup>.

The most peculiar aspect of the FM state in  $Gd_3SnC$  is the tricritical behaviour that appears near the boundary between the first- and the second-order phase transitions<sup>16</sup>. Figure 2c shows a modified Arrott plot<sup>17</sup> of the tricritical mean-field model for the FM order with  $\beta_{Arrott} = 0.25$  and  $\gamma_{Arrott} = 1$  in  $(H/M)^{1/\gamma_{Arrott}}$  and  $M^{1/\beta_{Arrott}}$ , respectively. Compared to other magnetic ordering models, it is apparent from the relative slopes (dashed red lines in Fig. 2c and Supplementary Fig. 2a–d) that the FM transition belongs to the universality class of the tricritical mean-field model (Fig. 2d). A clear crossover from a first-order to second-order transition is seen in the  $T$  dependent  $\rho$  and  $M$  curves under different  $H$  as shown in Fig. 2e,f, respectively. Three representative features in the data verify the crossover between FM orders: (i) disappearance of the peak in  $\rho$  at  $T_C$ , (ii) suppression of the hysteresis in the  $\rho-T$  curve during a thermal cycle (insets of Fig. 2e), and (iii) smooth increase of  $M$  upon cooling (Fig. 2f). Such tricritical behaviour often emerges in heavy-fermion systems such as  $UGe_2$ <sup>18</sup> and  $YbRh_2Si_2$ <sup>19</sup> due to the competition between Kondo coupling ( $T_K$ ) and Ruderman–Kittel–Kasuya–Yosida interaction<sup>20</sup>.

**Heavy-fermions with non-Fermi liquid behaviour.** More unusual properties of  $Gd_3SnC$  may be found in the heat capacity ( $C$ ) measurement results (Fig. 3). As a way to determine the unexpected behaviour, we compare the  $C$  of  $Gd_3SnC$  to those of FM Gd metal and non-magnetic  $La_3SnC$  antiperovskite, as shown in Fig. 3a. In contrast to the small  $C$  values of Gd metal and  $La_3SnC$  antiperovskite in the low- $T$  region, an extremely large  $C$  value with a Sommerfeld coefficient ( $\gamma$ ) of  $\sim 1114 \text{ mJ mol}^{-1} \text{ K}^{-2}$  at 90 mK is observed for the  $Gd_3SnC$ . The dramatic low- $T$  rise of  $C$  is reminiscent of a nuclear Schottky anomaly, most likely from the Sn nucleus (the natural abundance for non-zero nuclear spin  $^{13}C$  is below 1%). However, our modelling, which considers 16 % natural abundance of  $^{117}Sn$  and  $^{119}Sn$ , rules out the Schottky anomaly by showing that the required internal field is about  $\sim 1287 \text{ kOe}$ , a value much larger than any reported values<sup>21–23</sup> (Supplementary Fig. 4d). In addition, the Gd nuclear spin cannot be the culprit as we do not see a similar rise in  $C$  for Gd metal. Therefore, we attribute the logarithmic rise of  $C$  for  $Gd_3SnC$  below  $\sim 0.12 \text{ K}$  (Supplementary Fig. 4a) to a non-Fermi liquid (NFL) behaviour of itinerant conduction electrons<sup>24–</sup>

<sup>26</sup> (inset of Fig. 3a). A  $T$ -linear dependence of  $\rho$  in the low- $T$  region also supports the NFL behaviour of itinerant conduction electrons in  $\text{Gd}_3\text{SnC}$  (left panel in Fig. 3b). The transition from  $T$ -linear to  $T^2$  behaviour of  $\rho$  upon applying 140 kOe (right panel in Fig. 3b and Supplementary Fig. 5) is suggestive of a magnetic origin of the NFL behaviour<sup>27,28</sup>. Thus, we assume that an exotic quantum phenomenon coupled with a correlation between itinerant and localized electrons in the  $\text{Gd}_3\text{SnC}$  antiperovskite appears as heavy fermions.

As Gd f-electron levels locate deep in the binding energy, the heavy-fermion with the NFL behaviour should originate from the electrons of other orbitals, which is revealed from the analysis of the  $C$  of FM  $\text{Gd}_3\text{SnC}$ . The magnetic contribution ( $C_{\text{mag}}$ ) to the  $C$  of FM  $\text{Gd}_3\text{SnC}$  is obtained by subtracting the  $C$  of non-magnetic  $\text{La}_3\text{SnC}$  without 4f-electrons (La metal with the configuration of  $[\text{Xe}]4f^05d^16s^2$ ) from those of  $\text{Gd}_3\text{SnC}$  with seven 4f-electrons (Gd metal with the configuration of  $[\text{Xe}]4f^75d^16s^2$ ). We find two distinct features in  $C_{\text{mag}}$ : a large  $C_{\text{mag}}$  in the high- $T$  region ( $C_{\text{mag,high}}$ , Fig. 3c) and a small  $C_{\text{mag}}$  in the low- $T$  region ( $C_{\text{mag,low}}$ , inset of Fig. 3c). While the  $C_{\text{mag,high}}$  is attributed to the FM order of 4f<sup>7</sup>-electrons, which agrees well with the prediction of the renormalization-group approach<sup>29</sup> in the scheme of tricritical ferromagnetism (Supplementary Fig. 2f), the origin of  $C_{\text{mag,low}}$  is ambiguous. From the  $T$ -dependent magnetic entropy ( $\Delta S$ ) obtained by integrating  $C_{\text{mag}}(T)$  (Supplementary Fig. 4b), we can assign which electrons are responsible for  $C_{\text{mag,low}}$ . Figure 3d shows a large difference in  $\Delta S$  between the high- and low- $T$  regions:  $0.5R\ln 8$  and  $0.05R\ln 2$ , respectively. Since  $0.5R\ln 8$  reflects the contribution from seven 4f-electrons (4f<sup>7</sup>) involved in FM ordering, one may notice that the much smaller value of  $0.05R\ln 2$  has no correlation with 4f-electrons but is ascribed to 5d-electrons, which are responsible for the heavy-fermion with the NFL behaviour.

**Dual character of Gd 5d electrons.** This unconventional and anomalous d-electron heavy-fermion state in f-block Gd-based  $\text{Gd}_3\text{SnC}$  is, if true, the first case of FM-assisted heavy-fermion behaviour in 5d-electron systems. Density functional theory (DFT) calculations along with angle-resolved photoemission spectroscopy (ARPES) measurements provide a clear picture for the formation of the heavy-fermion state, which is induced not by 4f-electrons but by 5d-electrons of Gd element in the context of mixed bonding characters of the antiperovskite structure. Figure 4a shows ARPES data along the  $\Gamma$ -X- $\Gamma$  direction taken above (125 K) and below (90 and 13 K) the  $T_C$ . The 125 K data shows a fast-dispersing band centred at the X point. As the  $T$  is lowered to 90 K, the band shifts down due to the exchange splitting of both 4f- and 5d-electrons (Supplementary Fig. 6d). In addition to the fast-dispersing band (green curve), there is a weakly dispersing band near  $E_F$  (red curve in Fig. 4a, Supplementary Fig. 6a-c). Upon cooling to 13 K, the fast-dispersing band shifts further down, and the weakly dispersing band near  $E_F$  disappears. These changes in the electronic structure might be related to the hybridization of fast and weakly dispersing bands below 20 K. The  $T$ -dependent electronic structure change is also seen in the  $k_x$ - $k_y$  plane of Fermi surface maps in Fig. 4b; the Fermi surface pocket becomes larger as the  $T$  decreases. This enlarged Fermi surface is a typical phenomenon as found in various heavy-fermion systems<sup>27,30-32</sup>. The

Loading [MathJax]/jax/output/CommonHTML/fonts/TeX/fontdata.js rates that the Gd 5d-orbitals are almost solely

responsible for the states near  $E_F$ , while Sn 5p and C 2p derived states are located away from  $E_F$  (Fig. 4c). Meanwhile, we confirm that the contribution of Gd 4f-orbitals into the band structure near  $E_F$  is negligible but responsible for the FM ordering (Supplementary Fig. 7).

We note that the calculated band structure shows an anomalous flat band feature near  $E_F$ , which is also a signature of heavy-fermion behaviour (Fig. 4d,e). The experimentally observed flatness of the fast-dispersing band at the X point (13 K in Fig. 4a) is indeed well-reproduced by band calculations (highlighted as yellow colour in Fig. 4e). The fat band analysis reveals that the band hybridization triggers the appearance of a flat band feature near  $E_F$ . Importantly, the two hybridized bands originate from the only Gd 5d-orbitals:  $t_{2g}$  bands from the Gd–Gd bonds (red curves) and  $e_g$  bands from the mostly Gd–C bonds (green curves). Thus, we believe that the flat  $t_{2g}$  band observed at 90 K (Fig. 4a) is lifted above  $E_F$  after the band hybridization process (Supplementary Fig. 6e). Finally, we emphasize the importance of antiperovskite structure with mixed bonding nature, which is the key to imparting the unusual heavy-fermion behaviour to Gd<sub>3</sub>SnC. The crystal orbital Hamiltonian population (COHP) analysis (Fig. 4f) explains how the chemical bonds of CGd<sub>6</sub> octahedra in antiperovskite structure can induce the unusual band structure. The COHP analysis suggests two types of orbital overlap: a small orbital overlap in metallic Gd–Gd bond responsible for the  $t_{2g}$  bands near  $E_F$  (– ICOHP  $\sim$  0.5 eV/bond, Supplementary Table 2) and large orbital overlap in covalent Gd–C bond for the  $e_g$  bands below  $E_F$  (– ICOHP  $\sim$  1.5 eV/bond). This mixed bonding nature with the different degrees of orbital overlap leads to the unusual band dispersion of Gd 5d-electrons, as illustrated in Fig. 4g – i. Thus, the duality of Gd 5d-electrons participating in the mixed chemical bonds in CGd<sub>6</sub> octahedra of the Gd<sub>3</sub>SnC antiperovskite structure is a key factor that determines the unusual physical properties.

## Summary

In summary, we discovered the d-electron heavy-fermion state in the f-electron FM Gd<sub>3</sub>SnC antiperovskite. The mixed bonding nature of the antiperovskite structure, composed of metallic Gd–Gd bonds and covalent Gd–C bonds, is found to be the key ingredient for realizing the heavy-fermions of Gd 5d-electrons. The present findings are against the knowledge that the FM lanthanide elements are not suitable for heavy-fermion states, implying that the properties of the elements in the common crystal structure can be completely changed by adopting the antistructured lattice framework. This work will trigger further exploratory studies on the antistructures to challenge the common knowledge in the elemental properties of materials.

## Methods

**Crystal growth and structural analysis.** Stoichiometric Polycrystalline Gd<sub>3</sub>SnC ingot rods were used for the single-crystal growth by the floating zone (FZ) melting method. We mixed Gd, Sn metals, and graphite chips in a 3:1:1 molar ratio to fabricate a polycrystal ingot rod. The mixed sample was melted using the Loading [MathJax]/jax/output/CommonHTML/fonts/TeX/fontdata.js (> 99.9999%). The single crystal was grown by

four-mirror FZ melting method with the rod-shaped ingots under high purity argon (Ar > 99.9999%) with pressurized conditions in 0.3 MPa. The feed and the seed rod were rotated at 50 rpm, and the growing speed was 2 mm per hour. The crystal structure was determined using the high-resolution X-ray diffractometer and Rietveld analysis using the GSAS-II program.

**Physical property measurements.**  $\rho$ ,  $M$ , and  $C$  measurements were performed using a physical property measurement system (PPMS). The  $\rho$  and  $C$  at ambient pressure were measured down to 0.06 K using a diluted helium-3 refrigerator. To measure the electrical properties of samples, the electrical contacts in the four-probe configuration were adopted that made by Ag epoxy onto a sample. To prevent movement of samples by  $H$  (up to 140 kOe) in the chamber, samples were fixed using torr seal epoxy onto the PPMS puck. To measure the  $M$  of the sample, a vibrating sample magnetometer (VSM) was used. For  $C$  measurement, the standard relaxation method was adopted. Every process was performed in an Ar-filled glove box, and N-grease covered samples for  $\rho$  and  $C$  measurements to prevent degradation of Gd<sub>3</sub>SnC under ambient oxygen and water vapour atmosphere.  $T$ -dependent ARPES measurements were performed at the MERLIN beamline 4.0.3 of the Advanced Light Source, Lawrence Berkeley National Laboratory using both linearly horizontal ( $\pi$ ) and vertical ( $\sigma$ ) polarization from an elliptically polarized undulator. Spectra were acquired with a Scienta R8000 (BL 4.0.3) electron analyser. Cleaving of the samples was conducted at 13 K in an ultra-high vacuum better than  $5 \times 10^{-11}$  Torr. The total energy resolution of approximately 15 meV was used for measurements at  $h\nu = 142$  eV.

**DFT Calculations.** First-principles DFT calculations were performed using the generalized gradient approximation with the Perdew-Burke-Ernzerhof functional with spin-orbit coupling (SOC) and the projector augmented plane-wave method implemented in the Vienna *ab initio* simulation program code<sup>33-35</sup>. The 4f-, 5s-, 5p-, 5d- and 6s-electrons of Gd, the 5s- and 5p-electrons of Sn, and the 2s- and 2p-electrons of C were used as valence electrons. The plane-wave-basis cut-off energy was set to 600 eV. On-site Coulomb interaction values of  $U = 3$  eV were used for the Gd 5d-electrons (Supplementary Fig. 7). Self-consistency was carried out using an  $a \times b \times c$  unit cell containing 5 atoms, and a  $12 \times 12 \times 12$   $k$ -point mesh was used. Structural relaxation was performed until the Hellmann-Feynman forces were less than  $1 \times 10^{-5}$  eV  $\text{\AA}^{-1}$ , respectively. The crystal structures and charge density distribution were visualized with the Visualization for Electronic and Structural Analysis code<sup>36</sup>.

## Declarations

### Data Availability

The data that support the plots in this paper and other findings of this study are available from the corresponding author upon reasonable request.

### Acknowledgments

This work was supported by the Institute for Basic Science (IBS-R011-D1, IBS-R009-G2) and the National Research Foundation of Korea (NRF) grant funded by the Korean government (Ministry of Science, ICT & Future Planning) (No. 2015M3D1A1070639, NRF-2019R1I1A1A01061913) and. We acknowledge Dr. Filip Ronning (Los Alamos National Laboratory) for valuable discussions.

## Author Contributions

S.W.K. conceived the idea and organized the research. J.P. synthesized samples and measured physical properties. M.K and C.K. performed ARPES measurements. J.B, J.P, and K.L. analysed the structural and physical properties. J.B carried out computational studies. All the authors discussed the results and wrote the manuscript.

## Competing interests

The authors declare no competing interests.

## Additional Information

**Supplementary information** is available for this paper at <https://doi.org/xxxxx>.

**Correspondence** and requests for materials should be addressed to S.W.K.

**Peer review information** *Nature Materials* thanks XXXX and the other, anonymous, reviewer(s) for their contribution to the peer review of this work.

**Reprints and permission information** is available at <http://www.nature.com/reprints>.

**Publisher's note:** Springer Nature remains neutral with regard to jurisdictional claims in published maps and institutional affiliations.

## Rights and permissions

Reprints and Permissions

## References

1. Jeon, S. *et al.* Landau quantization and quasiparticle interference in the three-dimensional Dirac semimetal  $\text{Cd}_3\text{As}_2$ . *Nat. Mater.* **13**, 851–856 (2014).
2. Liu, Z. K. *et al.* A stable three-dimensional topological Dirac semimetal  $\text{Cd}_3\text{As}_2$ . *Nat. Mater.* **13**, 677–681 (2014).
3. Neupane, M. *et al.* Observation of a three-dimensional topological Dirac semimetal phase in high-mobility  $\text{Cd}_3\text{As}_2$ . *Nat. Commun.* **5**, 3786 (2014).

4. Liang, T. *et al.* Ultrahigh mobility and giant magnetoresistance in the Dirac semimetal Cd<sub>3</sub>As<sub>2</sub>. *Nat. Mater.* **14**, 280–284 (2015).
5. Uchida, M. *et al.* Ferromagnetic state above room temperature in a proximitized topological Dirac semimetal. *Phys. Rev. B* **100**, 245148 (2019).
6. He, L. *et al.* Pressure-induced superconductivity in the three-dimensional topological Dirac semimetal Cd<sub>3</sub>As<sub>2</sub>. *npj Quantum Mater.* **1**, 16014 (2016).
7. Wang, Y. *et al.* Antiperovskites with exceptional functionalities. *Adv. Mater.* **32**, 1905007 (2020).
8. Huang, D. *et al.* Unusual valence state in the antiperovskites Sr<sub>3</sub>SnO and Sr<sub>3</sub>PbO revealed by x-ray photoelectron spectroscopy. *Phys. Rev. Mater.* **3**, 124203 (2019).
9. Ma, Y. *et al.* Realization of epitaxial thin films of the topological crystalline insulator Sr<sub>3</sub>SnO. *Adv. Mater.* **32**, 2000809 (2020).
10. Bannikov, V. V, Shein, I. R. & Ivanovskii, A. L. Structural, elastic and electronic properties of new antiperovskite-like ternary nitrides AlNNi<sub>3</sub>, GaNNi<sub>3</sub> and InNNi<sub>3</sub> as predicted from first principles. *Comput. Mater. Sci.* **49**, 457–461 (2010).
11. Gesing, T. M., Wachtmann, K. H. & Jeitschko, W. The perovskite carbides A<sub>3</sub>MC (A = Sc, Y, La-Nd, Sm, Gd-Lu; M = Al, Ga, In, Tl, Sn, Pb). *Zeitschrift für Naturforsch. B* **52**, 176–182 (1997).
12. Nigh, H. E., Legvold, S. & Spedding, F. H. Magnetization and electrical resistivity of gadolinium single crystals. *Phys. Rev.* **132**, 1092–1097 (1963).
13. Steppke, A. *et al.* Ferromagnetic quantum critical point in the heavy-fermion metal YbNi<sub>4</sub>(P<sub>1-x</sub>As<sub>x</sub>)<sub>2</sub>. *Science* **339**, 933–936 (2013).
14. Krellner, C. *et al.* Ferromagnetic quantum criticality in the quasi-one-dimensional heavy fermion metal YbNi<sub>4</sub>P<sub>2</sub>. *New J. Phys.* **13**, 103014 (2011).
15. Lee, S. Y. *et al.* Ferromagnetic quasi-atomic electrons in two-dimensional electride. *Nat. Commun.* **11**, 1526 (2020).
16. Huang, K. *Statistical mechanics* (John Wiley & Sons, 1987).
17. Arrott, A. Criterion for ferromagnetism from observations of magnetic isotherms. *Phys. Rev.* **108**, 1394–1396 (1957).
18. Taufour, V., Aoki, D., Knebel, G. & Flouquet, J. Tricritical point and wing structure in the itinerant ferromagnet UGe<sub>2</sub>. *Phys. Rev. Lett.* **105**, 217201 (2010).
19. Misawa, T., Yamaji, Y. & Imada, M. YbRh<sub>2</sub>Si<sub>2</sub>: Quantum tricritical behavior in itinerant electron systems. *J. Phys. Soc. Japan* **77**, 093712 (2008).
20. Misawa, T., Yamaji, Y. & Imada, M. Spin fluctuation theory for quantum tricritical point arising in proximity to first-order phase transitions: Applications to heavy-fermion systems, YbRh<sub>2</sub>Si<sub>2</sub>, CeRu<sub>2</sub>Si<sub>2</sub>, and β-YbAlB<sub>4</sub>. *J. Phys. Soc. Japan* **78**, 084707 (2009).
21. Bosch, D., Pobell, F. & Kienle, P. Magnetic fields at <sup>119</sup>Sn in rare earth metals. *Phys. Lett.* **22**, 262–264 (1966).

22. Gotthardt, V., Möller, H. S. & Mössbauer, R. L. Magnetic field at  $^{119}\text{Sn}$  in gadolinium. *Phys. Lett. A* **28**, 480–481 (1969).
23. Parish, R. V. *The Interpretation of  $^{119}\text{Sn}$ -Mössbauer Spectra*. (Wiley-Intersci. New York, 1972).
24. Seaman, C. L. *et al.* Evidence for non-Fermi liquid behavior in the Kondo alloy  $\text{Y}_{1-x}\text{U}_x\text{Pd}_3$ . *Phys. Rev. Lett.* **67**, 2882–2885 (1991).
25. Stewart, G. R. Non-Fermi-liquid behavior in d- and f-electron metals. *Rev. Mod. Phys.* **73**, 797–855 (2001).
26. Gegenwart, P., Si, Q. & Steglich, F. Quantum criticality in heavy-fermion metals. *Nat. Phys.* **4**, 186–197 (2008).
27. Shen, B. *et al.* Strange-metal behaviour in a pure ferromagnetic Kondo lattice. *Nature* **579**, 51–55 (2020).
28. Custers, J. *et al.* The break-up of heavy electrons at a quantum critical point. *Nature* **424**, 524–527 (2003).
29. Bagnuls, C. & Bervillier, C. Nonasymptotic critical behavior from field theory at  $d = 3$ : The disordered-phase case. *Phys. Rev. B* **32**, 7209–7231 (1985).
30. Coleman, P. *Introduction to many-body physics*. (Cambridge University Press, 2015).
31. Wirth, S. & Steglich, F. Exploring heavy fermions from macroscopic to microscopic length scales. *Nat. Rev. Mater.* **1**, 16051 (2016).
32. Zhang, Y. *et al.* Emergence of Kondo lattice behavior in a van der Waals itinerant ferromagnet,  $\text{Fe}_3\text{GeTe}_2$ . *Sci. Adv.* **4**, eaao6791 (2018).
33. Kresse, G. & Furthmüller, J. Efficient iterative schemes for *ab initio* total-energy calculations using a plane-wave basis set. *Phys. Rev. B* **54**, 11169–11186 (1996).
34. Blöchl, P. E. Projector augmented-wave method. *Phys. Rev. B* **50**, 17953–17979 (1994).
35. Perdew, J. P., Burke, K. & Ernzerhof, M. Generalized gradient approximation made simple. *Phys. Rev. Lett.* **77**, 3865–3868 (1996).
36. Momma, K. & Izumi, F. VESTA 3 for three-dimensional visualization of crystal, volumetric and morphology data. *J. Appl. Crystallogr.* **44**, 1272–1276 (2011).

## Figures

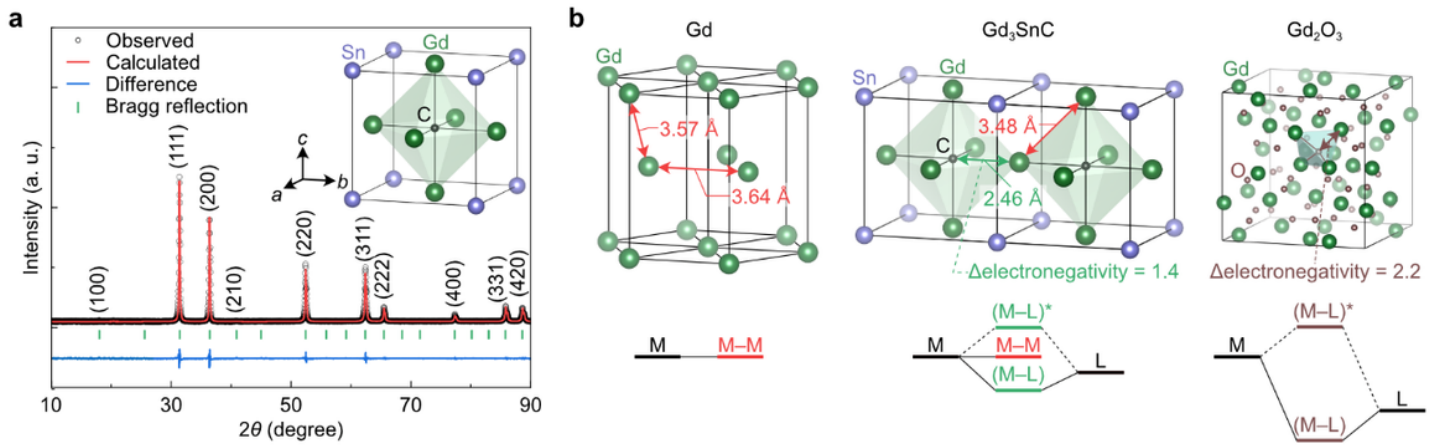


**Figure 1**

Crystal structure and mixed bonding nature of  $\text{Gd}_3\text{SnC}$  antiperovskite. a, Powder XRD pattern with Rietveld fitting of  $\text{Gd}_3\text{SnC}$ . The measurement was performed at room temperature. The inset depicts the crystal structure obtained from the Rietveld refinement result. b, Comparison of bonding features in Gd-based compounds. Red, green, and brown colours represent the metallic Gd–Gd (M–M), covalent Gd–ligand (M–L), and ionic Gd–ligand (M–L) bonds, respectively. The bond length of Gd–Gd and Gd–C bonds, and electronegativity difference ( $\Delta\text{electronegativity}$ ) between Gd and surrounding ligands are also shown in the crystal structures. Schematics of molecular orbital diagrams are shown in the lower panel. (M–L)\* represents the antibonding molecular orbital of M–L bonds.

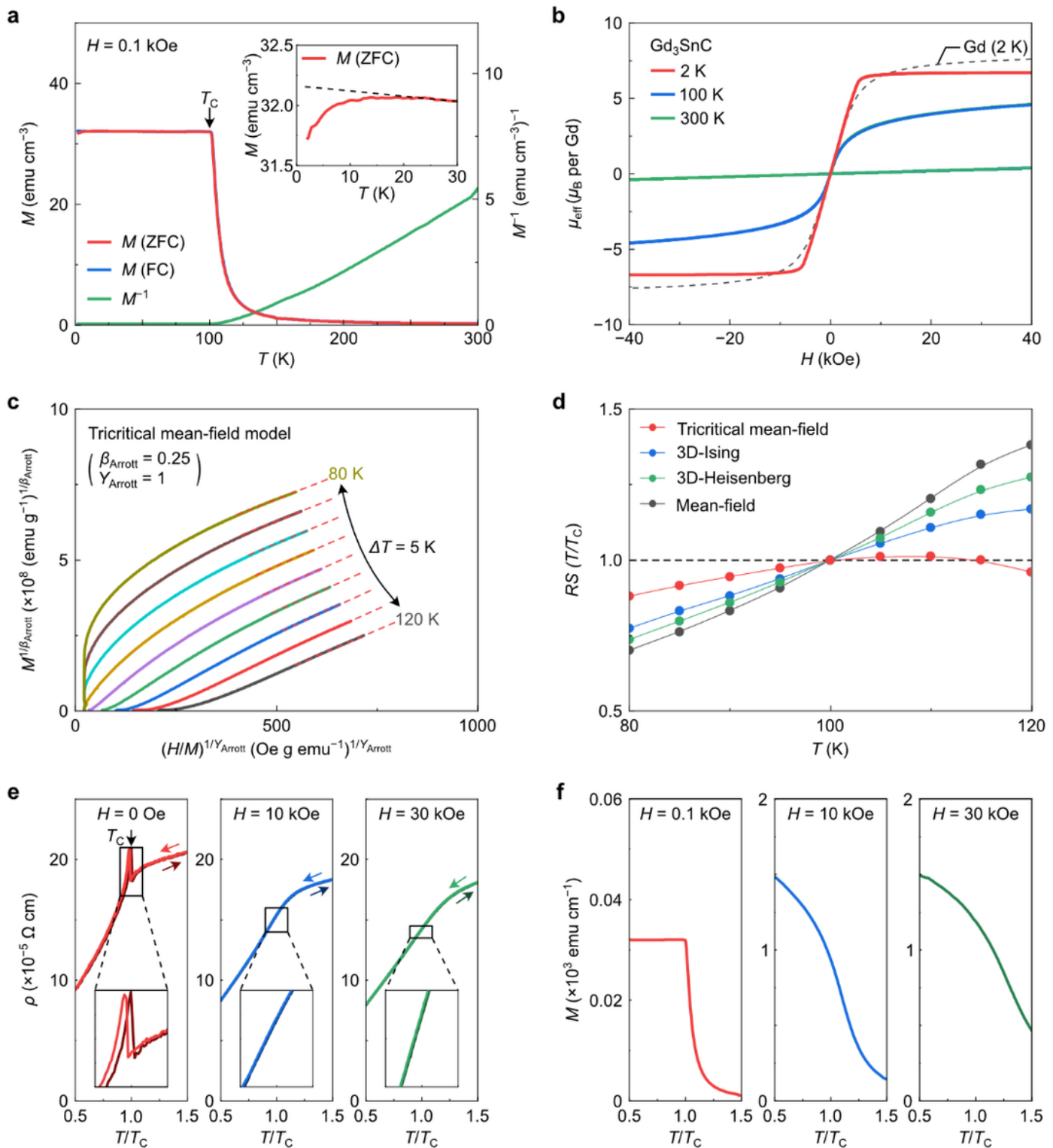


**Figure 2**

Tricritical ferromagnetic behaviour in  $\text{Gd}_3\text{SnC}$  antiperovskite. a, T-dependent  $M$  under zero-field cooling (ZFC) and field cooling (FC) conditions. Inverse magnetization ( $M^{-1}$ ) for FC result is also illustrated. The inset shows an enlarged view of the ZFC curve at low  $T$ . Dashed black line is a guide for the eyes. b, H-dependent effective magnetic moment ( $\mu_{\text{eff}}$ ) per Gd atom at various  $T$ .  $\mu_{\text{eff}}-H$  curve for Gd metal

Loading [MathJax]/jax/output/CommonHTML/fonts/TeX/fontdata.js (black curve). c, Modified Arrott plot for the tricritical

mean-field model. Modified Arrott plots for other models are presented in Supplementary Fig. 2a–d. The dashed red lines are linear fits for the high field regime. d, T-dependent relative slope (RS) curves near the TC for various models. e, Cooling and heating curves of T-dependent  $\rho$  for various H values. f, M–T curves for various H values.

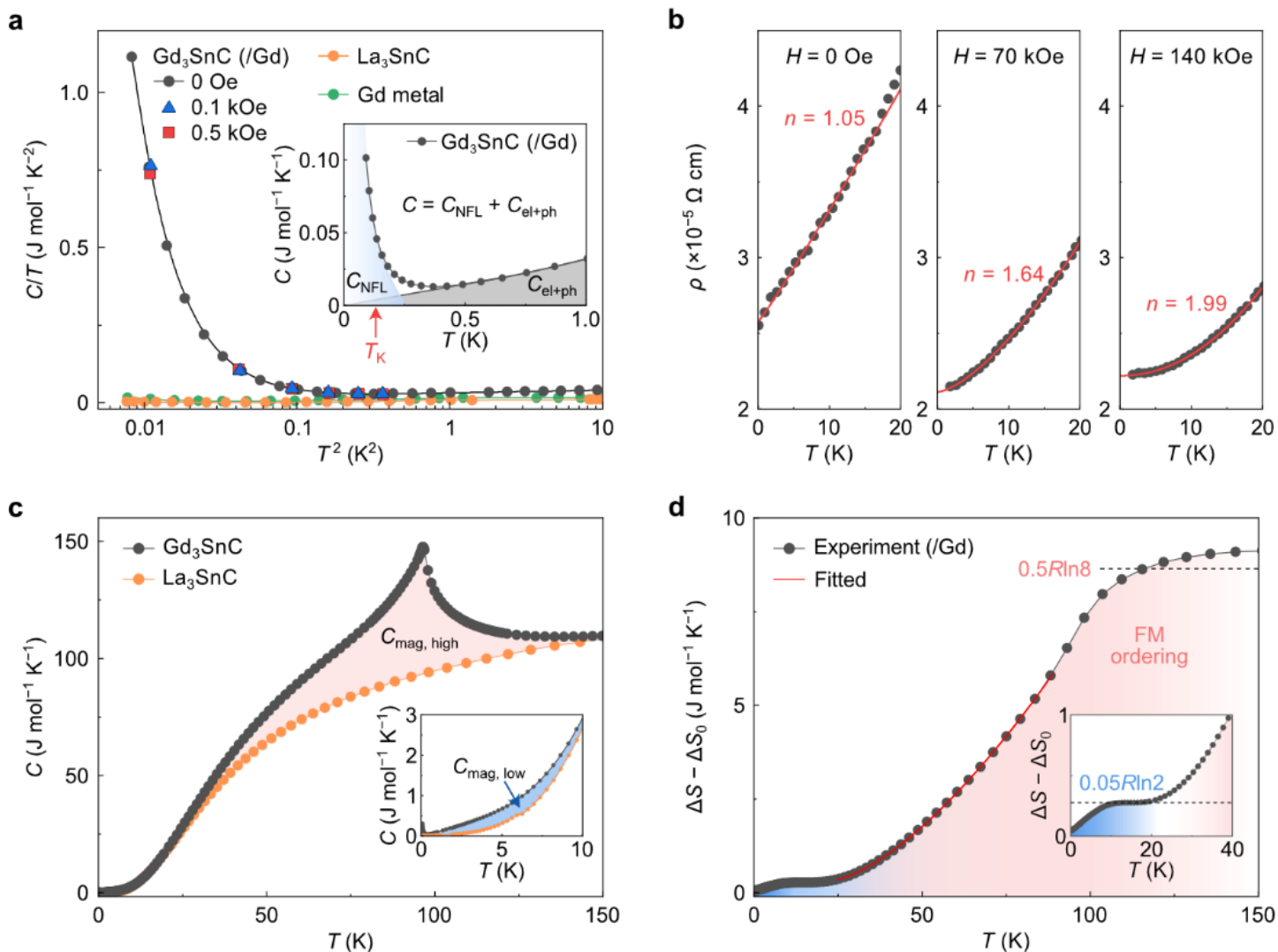


**Figure 3**

Unconventional heavy-fermion behaviour with non-Fermi-liquid behaviour in Gd<sub>3</sub>SnC antiperovskite. a,  $C/T$  versus  $T^2$  curves for antiperovskite Gd<sub>3</sub>SnC, isostructural La<sub>3</sub>SnC, and Gd metal. The  $C$  value of Gd<sub>3</sub>SnC corresponds to the heat capacity per mole of Gd. The inset shows a fitting result of  $C$  versus  $T$  curve of Gd<sub>3</sub>SnC using  $C_{\text{NFL}} = -A\ln T + B$  and  $C_{\text{el+ph}} = CT + DT^3$ , where  $C_{\text{NFL}}$  and  $C_{\text{el+ph}}$  are NFL and electron + phonon contributions, respectively.  $A$ ,  $B$ ,  $C$ , and  $D$  are constants. b, T dependent  $\rho$  at different  $H$ . Red curves are single power-law fits ( $\rho = \rho_0 + AT^n$ ) of the data. c,  $C$  versus  $T$  for Gd<sub>3</sub>SnC and La<sub>3</sub>SnC. The inset is an enlarged view of the low-T region.  $C_{\text{mag}}$  for Gd<sub>3</sub>SnC is estimated by subtracting the  $C$  of the non-magnetic La<sub>3</sub>SnC (Supplementary Fig. 4b). d, T-dependent  $\Delta S - \Delta S_0$  for Gd<sub>3</sub>SnC per mole of Gd.

$\Delta S_0$  is the residual entropy. The red curve represents the FM contribution obeying  $\Delta S - \Delta S_0 = \int (aT^{3/2} + b)/T dT$ , where  $a$  and  $b$  are constants. The inset shows a magnified view below 40 K.

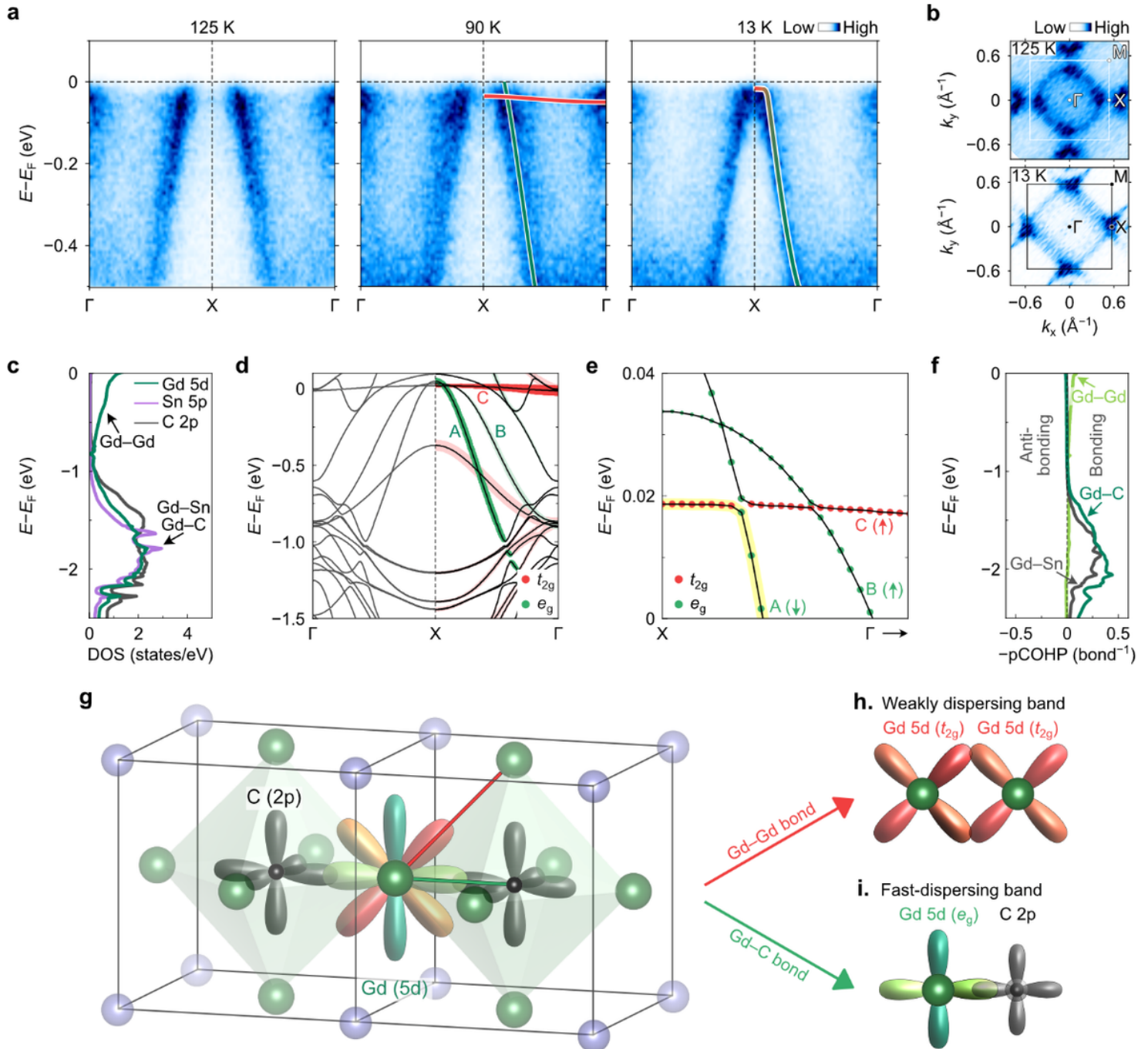


**Figure 4**

Electronic structure of heavy-fermion Gd<sub>3</sub>SnC antiperovskite. a, ARPES spectra along the  $\Gamma$ -X- $\Gamma$  direction at 125, 90, and 13 K. Green and red solid curves indicate fast-dispersing band and weakly dispersing band, respectively. Details on the energy distribution curves (EDCs) are shown in Supplementary Fig. 6. b, Fermi surface topology in the  $k_x$ - $k_y$  plane from ARPES measurements at 125 and 13 K. White and black squares represent the first Brillouin zone. c, Calculated partial DOS. d, Calculated band structure along the  $\Gamma$ -X- $\Gamma$  direction with fat band analysis, exhibiting the  $t_{2g}$  (red colour) and  $e_g$  (green colour) contributions

Loading [MathJax]/jax/output/CommonHTML/fonts/TeX/fontdata.js

of Gd 5d-orbitals. Band thickness represents the contribution of each orbital. e, Near Fermi energy band structure around the X point, showing a band hybridization between fast-dispersing and weakly dispersing bands. f, Partial COHP (pCOHP) for Gd–Gd, Gd–C, and Gd–Sn bonds. pCOHP for other bonds can be found in Supplementary Fig. 8. g–i, Schematic illustration of the mixed bonding state for Gd 5d-orbitals.

## Supplementary Files

This is a list of supplementary files associated with this preprint. Click to download.

- [20210317Gd3SnCSupplementary.docx](#)